Cardiovascular Engineering and Technology, Vol. 3, No. 4, December 2012 *(© 2012)* pp. 402–412
DOI: 10.1007/s13239-012-0111-9

Comparative Evaluation of Mitral Valve Strain by Deformation Tracking in 3D-Echocardiography

S. Ben Zekry,[1] G. Lawrie,[1] S. Little,[1] W. Zoghbi,[1] J. Freeman,[2] A. Jajoo,[2] S. Jain,[2] J. He,[2] A. Martynenko,[2] and R. Azencott[2,3]

[1]The Methodist Hospital Research Institute, Houston, TX, USA; [2]Department of Mathematics, University of Houston, Houston, TX, USA; and [3]C.M.L.A. Ecole Normale Superieure, Cachan, France

(Received 7 October 2011; accepted 12 October 2012; published online 26 October 2012)

Associate Editor Ajit P. Yoganathan oversaw the review of this article.

Abstract—We present new algorithms to compute patient specific strain maps for mitral valve leaflets, by tracking and modeling deformations of the mitral valve apparatus in 3D echocardiography. We can then quantify comparisons of mitral leaflets strain maps between normal patients and cases of mitral valve prolapse or regurgitation. For patients with mitral valve regurgitation, we compare mitral leaflets strain maps between pre-surgery and post-surgery, to quantify the strain reduction due to mitral valve repair surgery.

Keywords—Diffeomorphic tracking, Deformable shapes, Human mitral valve, 3D-echocardiography, Leaflet tissue strain.

MAIN GOALS

Background

3D-Echocardiographic image sequences (3D-Echo) provide clinicians with visual evidence of mitral valve dysfunction, such as organic regurgitation and mitral leaflets prolapse. When patients undergo valve repair surgery, post-operative 3D-Echo can help surgeons to visualize the functional impact of surgery. Analysis of ultrasound images of the mitral valve has often been used to study the areas of regurgitation zones in pre-surgery patients.[1,11,14] More generally, 3D-Echo image data have been studied by registration techniques to reconstruct cardiac deformations.[13,18,25,28,35]

More specific finite elements modeling of the mitral valve deformations have been generated and studied for ovine and porcine models, based on *in vivo* open hearts experiments.[21,22,24,31]

Generally these finite elements models have focused on the numerical emulation of dynamic elasticity models of the mitral valve leaflets.[22,24] The typical goals was to parametrize these elaborate and semi-realistic elasticity models on the basis of *in vivo* and *in vitro* animal model experimental data, and to then use the parametrized elasticity models to compute stress values for the mitral leaflets.

For human mitral valves, this type of dynamic modeling task is seriously complicated by the lack of equivalent *in vivo* quantitative open heart experimental data focused on the mitral valve.

Scope of the Present Study

Hence in our study, which relies only on non-invasive ultrasound data analysis for *human mitral valves*, we have deliberately avoided to compute or simulate sophisticated elasticity models of the observed mitral valves. We have focused instead on patient specific mitral leaflets strain computations, and on strain comparisons across patients or before and after mitral valve repair surgery.

We present new computerized algorithmics to track and quantify the dynamic deformations of the Mitral Valve Apparatus (MVA) from 3D-Echo image data sets. This patient specific 3D-reconstruction of MVA geometry and dynamics allows the computation of detailed strain maps for the two mitral leaflets at end systole.

We can then quantitatively compare mitral leaflets strain maps between normal patients and patients with mitral valve prolapse and/or regurgitation.

We also implement patient specific statistical comparisons of mitral leaflets strain maps between pre- and post-surgery, which can be used to quantify, on a case

Address correspondence to R. Azencott, Department of Mathematics, University of Houston, Houston, TX, USA. Electronic mail: razencot@math.uh.edu

by case basis, the strain reductions achieved by surgical valve repair.

METHODS: PATIENT POPULATION

At The Methodist Hospital (TMH, Cardiology), this study, approved by the human research review board of TMH, enrolled 20 patients who provided written informed consent: 10 normal patients with no structural heart disease, and 10 patients with mitral valve prolapse and significant regurgitation, already scheduled for NRD surgery (Non-Resectional Dynamic mitral valve repair). NRD surgery keeps leaflets and annulus intact, but reduces the annulus by suture of a flexible ring.[26,27]

METHODS: 3D-ECHOCARDIOGRAPHY PROTOCOL

To visualize the MVA dynamics, Transesophageal 3D-Echo data sets were acquired for all patients by mid-esophageal full volume echocardiography, with an IE-33 Philips ultrasound system and X7-2t probe, at approximately 25 image frames/s. Each such DICOM 3D-image data file recorded a sequence of about thirty 3D-images of beating hearts. Each 3D-image frame had a resolution of $208 \times 224 \times 208$ voxels, with typical voxel size $0.5 \times 0.5 \times 0.5$ mm^3.

We thus acquired one DICOM image file per normal patient, and two such image files per patient with MV regurgitation, namely one before NRD surgery and one after NRD surgery.

METHODS: INTERACTIVE TAGGING

Each DICOM 3D image file was uploaded to SLICER 3D, a freeware 3D-display environment, for interactive tagging by a cardiology clinician, using a tagging software module developed by us.

We have focused on four MVA components: the anterior and posterior leaflets AL and PL, viewed as two thin surfaces enclosed by a thin ring (the mitral annulus MA) and by the coaptation line (COAPT), along which leaflets close the valve during systole (see Fig. 3). To tag the MVA on any 3D image frame, we select a rotation axis ROT roughly orthogonal to the main principal components plane associated to the MVA, and passing through the tip *AntHorn* of the annulus anterior horn. About 50 planes $P_1 \ldots P_{50}$ containing the axis ROT, were then selected by small successive rotations around ROT, to span the entire leaflets AL and PL (see Figs. 1, 2). Within each plane P_n, the tags included the intersection points of P_n with the coaptation line and the annulus, plus 5–10 points on each leaflet. For each tag T in P_n we define the polar coordinates r, θ of T as the distance r between *AntHorn* and T, and the angle $\theta = \theta_n$ between planes P_1 and P_n.

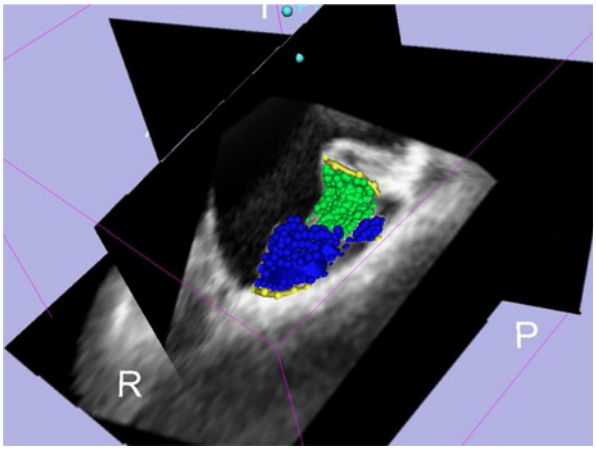

FIGURE 1. Interactive tagging in the SLICER 3D environment. The green dots represent tagged points of the anterior leaflet (AL), while the blue points represent tagged points of the posterior leaflet (PL).

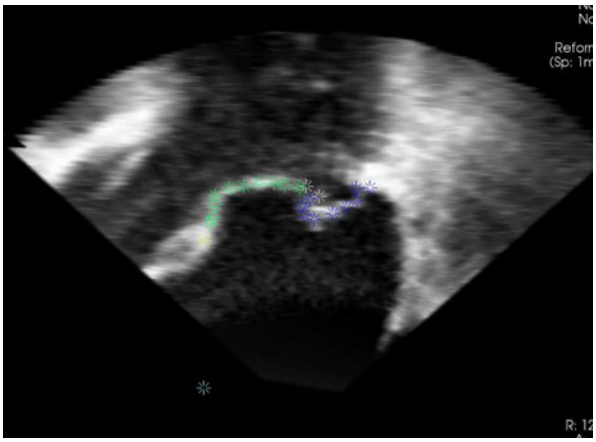

FIGURE 2. A sample tagging plane P_i (see below). The color scheme is that of Fig. 1.

For post-surgery patients, the tagging was focused on the anterior and posterior leaflets zones enclosed by the flexible surgical ring.

This tagging was performed at MidSystole (MS) and EndSystole (ES), to pin down two reliable reference positions for each one of the four MVA components.

We point out that during these two tagging operations, we do not need, and hence we do not attempt, to maintain any precise (or even imprecise) matching between the tags at time MS and those at time ES (Fig. 3).

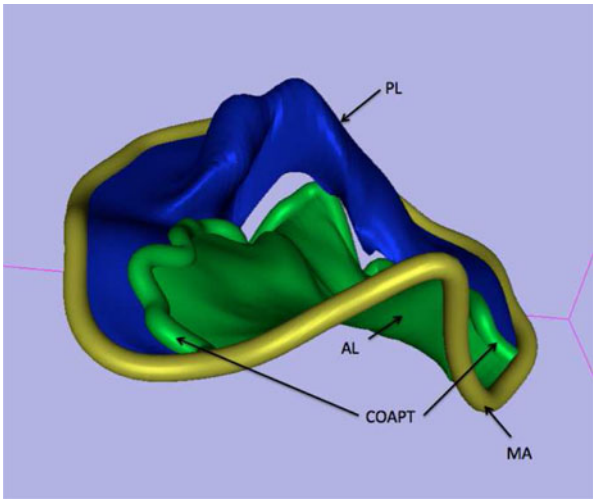

FIGURE 3. Patient specific MVA model (a regurgitation case). The yellow tube represents the MA, while the green tube represents the coaptation zone/AL edge. The green leaflet is the AL, while the blue leaflet is the PL.

METHODS: STATIC MODELING OF MVA COMPONENTS

For each 3D-Echo DICOM file, the MVA tags recorded at MS and ES are exported to a MATLAB environment. Here we compute patient specific smooth geometric models of the MVA components, with each component being modeled as a deformable smooth shape in R^3.

For each patient and each reference frame, we had about 60 tags on the MA, 40 tags on the COAPT, plus one cloud of about 200 tags for each leaflet. Principal Components Analysis (PCA) of these two clouds of points generates two new orthonormal bases in R^3, and thus two new coordinate systems (x, y, z) and (X, Y, Z), one per leaflet.

For *each normal or post-surgery* patient, the leaflets surfaces AL and PL were separately fitted by single cartesian equations, denoted

$$z = f_{\mathrm{AL}}(x, y) \quad \text{and} \quad Z = F_{\mathrm{PL}}(X, Y) \tag{1}$$

The functions f_{AL} and F_{PL} were modelled by *Bi-Cubic Splines (B-splines)*, which are linear combinations of specific polynomials of degree 3 with bounded supports.[30]

Recall that B-splines fitting of the equation $z = f_{\mathrm{AL}}(x, y)$ for instance minimizes the sum of squared errors of fit of this equation to the available data points plus a quadratic term controlling the smoothness of f_{AL}.[30] A preliminary fitting yields rough errors of fit, from which we derive tag weights; we then launch a final B-spline fitting modulated by these weights.

For *pre-surgery* patients with MV prolapse and regurgitation, the more complicated shapes of prolapsed leaflets present geometric obstructions to the preceding approach. So we model each leaflet by 3 parametric equations

$$x = u(r, \theta),\ y = v(r, \theta),\ z = w(r, \theta) \tag{2}$$

where u, v, w are patient specific B-splines functions of the polar coordinates r, θ defined above.

For fixed $\theta = \theta_n$, the intersections of AL and PL with plane P_n are fitted by two planar B-splines curves. Then for a finite family of radiuses $r = r_j$, the intersections of AL and PL with a spherical shell of radius r_j centered at *AntHorn* are fitted by two spherical B-splines curves. This "lofting" technique.[30] generates two grids of smooth curves (one grid per leaflet). Each grid is separately fitted by B-splines parametric Eq. (2).

Similar but simpler B-splines modeling was applied to generate smooth parametric equations

$$x = a(s),\ y = b(s),\ z = c(s) \tag{3}$$

for the annulus and for the coaptation line, where a, b, c are B-splines functions of the curve arc length s.

For all patients, these procedures provided smooth patient specific B-splines models of the four MVA components, at MS and ES, with individual errors of fit of the order of 1 mm.

METHODS: REGISTRATION OF 3D-ECHO IMAGE SEQUENCES

Registration of 3D-Echo images has been used to evaluate cardiac deformations, as in Heyde *et al.*[18] and Elen *et al.*[13] which estimate myocardium strain within the left ventricle.

Strain tensor computation based on 3D-echocardiography requires a reasonably accurate 3D-image sequence registration, which is a complicated task, since heart deformations tracking must confront non-linear and often large deformations between successive image frames. Multiple registration algorithms have been applied to echocardiographic image data, including optical flow, block matching, and spline based registration.

Early optical flow approaches exhibited mediocre performances.[5,6,34] Indeed they assumed pixel intensities to remain constant between consecutive image frames, and hence were highly sensitive to "speckle" noise, always present in ultrasound imaging.

The accuracy of block matching techniques[9,10,12,32,33] strongly depends on block size, and it is quite difficult to select block-sizes capturing simultaneously both large and small deformations.

Spline-based registration[25,28] have performed better for myocardial motion recovery, and are able to capture non-linear deformations, but their accuracy,

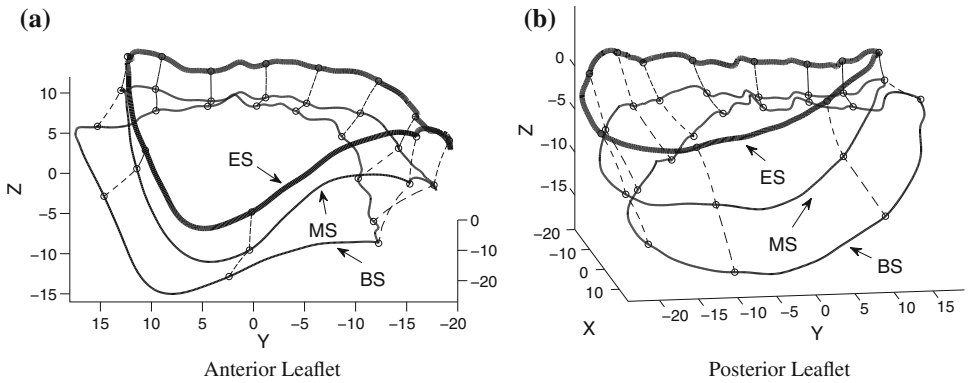

FIGURE 4. Normal case. Reconstructed leaflets deformations from beginning systole BS to end systole ES, based on 3 MVA snapshot models at times BS, MS, ES. (a) and (b) respectively display only the motion of the AL boundaries and of the PL boundaries. For AL as well as for PL, these boundaries include a segment of the annulus, and the coaptation line. Note that in our 20 patients study, we systematically used only 2 reference snapshots (at times MS and ES) and we reconstructed the leaflets deformations between MS and ES. We always had 5–6 available image frames between MS and ES.

which is reasonable for small deformations, becomes weaker for large deformations. A few studies[12,33,35] have explored maximum likelihood techniques, incorporating a Gaussian or a Rayleigh stochastic model for "speckle" noise, but they assume small deformations at each time frame, and require case specific statistical studies to parametrize correctly the "speckle" models.

Our focus was the precise 3D-tracking of two thin deformable surfaces with boundaries, namely the mitral leaflets bounded by the annulus and the coaptation line. We have chosen to model heart deformations by *diffeomorphisms* of R^3,[4,8,16,20] which are arbitrary invertible and continuously differentiable (or "smooth") deformations of R^3. This natural geometric requirement overcomes the limitations of "small deformations" registration by allowing computed heart deformations to be large and non-linear, while remaining smooth and invertible, which guarantees a good preservation of surfaces topologies. Moreover smoothness of reconstituted deformations is crucial to compute strain tensors, which involve space derivatives of deformations.

Classical 3D-volume image registration techniques cannot guarantee the invertibility of reconstructed deformations, contrary to our diffeomorphic registration, where invertibility is forced by our algorithmics, which automatically generates diffeomorphisms minimizing a natural cost function. Several other 3D-image elastic registration techniques do minimize volume based cost functions, involving sums of N^3 penalization terms, namely one per image voxel. But we focus here on registration quality for a much smaller number of voxels, namely the roughly N^2 voxels located on the thin leaflets surfaces S_t. So standard volume based cost functions are not sensitive enough to detect matching errors concentrated on our moving surfaces. These highly localized errors are much better controlled by our cost functions involving only the voxels of S_t (Fig. 4).

The computation of our diffeomorphic registration between times MS and ES has another advantage: it does not require at all the use of matched tagged landmarks between leaflets models at MS and ES.

METHODS: DIFFEOMORPHIC TRACKING OF LEAFLETS IN 3D-ECHO IMAGE SEQUENCES

Let $S(t)$ be a deformable shape in euclidean space R^3. Here $S(t)$ is either the annulus curve or the surface of one mitral valve leaflet. At times $t_0 < t < t_1$, we observe 3D-images displaying the successive positions of $S(t)$.

In this study, we had imposed $t_0 =$ MS and $t_1 =$ ES. The number of available image frames between MS and ES in our 3D-Echo data was typically 5 or 6 frames, including the two image frames at times MS and ES. The technical goal in this section is to reconstruct the deformations of the shape S_t between MS and ES.

Our diffeomorphic registration method below is however not limited to the case of 2 reference frames, and for instance we have also successfully tested this registration technique for cases where we had generated three reference snapshots, at times BS, MS, ES (see Figs. 4a, 4b).

Call $F_t(x)$ the position at time t of any initial point x in $S_0 = S(t_0)$. We then have $S(t) = F_t(S_0)$. As in Azencott *et al.*,[4] Beg *et al.*,[7] Miller *et al.*,[29] these dynamic deformations F_t are viewed here as diffeomorphisms of R^3, as mentioned above.

To compute the unknown diffeomorphisms F_t, it is far more efficient at the algorithmic level to first compute the unknown *deformation velocities* $V_t(z)$ indexed by the points z of R^3. These velocities can be viewed as time dependent smooth vector fields $V_t(z)$ on R^3. Once the unknown velocities $V_t(z)$ are computed,

we numerically reconstruct the deformations F_t by solving the following system of ordinary differential equations (ODE)

$$\frac{dF_t}{dt}(x) = V_t(F_t(x)) \quad \text{and} \quad F_{t_0}(x) = x \tag{4}$$

and the reconstructed deformations F_t will then necessarily be differentiable and invertible. To compute the unknown family $V = (V_t(z))$ of deformation velocities, we minimize a Cost Function $J(V)$ which penalizes the "defects" of the $V_t(z)$ and of the associated invertible deformations F_t. This cost function combines 3 penalization terms controlling 3 key deformation features

$$J(V) = \text{KIN}(V) + \lambda\, \text{SHM}(V) + \mu\, \text{ID}(V) \tag{5}$$

where λ and μ are fixed positive weights.

The "Kinetic Energy" KIN(V) of the deformation velocities $V_t(z)$ forces velocities to vary smoothly in z, and controls their sizes $||V_t(z)||$.

The "Shape Matching" term SHM (V) controls the accuracy of leaflet matching : it evaluates the geometric distance between the actual leaflet snapshot at terminal time t_1 = ES, and the approximating surface F_{t_1} (S_0) generated by computed deformation of the initial leaflet snapshot S_0.

The "Intensities Disparity" term ID (V) constrains the image intensities on leaflets surfaces to vary fairly continuously during deformations, (without forcing intensities to remain nearly constant).

We now outline the technical definitions of these 3 terms.

Kinetic Energy : As in Azencott *et al.*,[4] we want velocity fields $V_t(z)$ with finite kinetic energy to belong to a Hilbert vector space H of very smooth vector fields, namely the self-reproducing Hilbert space H generated by a fixed Gaussian kernel

$$K(x,y) = \exp(-||x-y||^2/2\tau^2)$$

where x and y are arbitrary vectors in R^3, and $\tau > 0$ is a fixed scale parameter. To this end, the kinetic energy KIN(V) is defined by

$$KIN(V) = \frac{1}{2}\int_{t_0}^{t_1} dt \int_{R^3}\int_{R^3} dxdy\; K(x,y) < V_t(x), V_t(y) >$$

where $< v\,, w >$ is the usual scalar product of 3D-vectors v and w.

Shape Matching : By tagging and B-splines model fitting, we have constructed for each 3D-Echo image sequence and each leaflet, two leaflet snapshots models $S_0 = S(t_0)$ and $S_1 = S(t_1)$, computed from the image data at instants t_0 = MS and t_1 = ES. For any candidate deformations F_t, we need to evaluate how well the deformed surface F_{t_1} (S_0) matches the reference surface S_1. So we quantify the distance between any two surfaces S and S' by their Hausdorff distance $d(S, S')$, which is defined by

$$d(S,S') = \max[D(S,S'), D(S',S)] \tag{6}$$

$$\text{where} \quad D(S,S') = \max_{x\in S}\min_{y\in S'} ||x-y|| \tag{7}$$

Any candidate family of velocity fields $V_t(z)$ determines a family of diffeomorphisms F_t of R^3 by resolution of the ODE system (4). Denote by $\hat{S}_1 = F_{t_1}(S_0)$ the deformation of S_0 by the diffeomorphism F_{t_1}. The shape matching disparity term SHM (V), is then defined by

$$SHM(V) = d(S_1, \hat{S}_1) \tag{8}$$

Intensities Disparity: The initial leaflet surface S_0 is discretized by a finite mesh M_0, including between 1500 and 3000 grid points. Let t and $t + 1$ be two successive instants in the finite set T of actual image frame times between t_0 and t_1. Echocardiographic data provide the 3D-image intensities $I_t(z)$ on a finite cube of voxels z. By spatial interpolation, we extend the intensity values $I_t(z)$ to any z in R^3.

The intensity disparity along deformation trajectories is then defined by

$$ID(V) = \sum_{t\in T}\sum_{x\in M_0} (I_{t+1}[F_{t+1}(x)] - I_t[F_t(x)])^2 \tag{9}$$

METHODS: NUMERICAL COMPUTATION OF DIFFEOMORPHIC SURFACE TRACKING

Among all families $V = V_t(z)$ of velocity fields we seek a V which *minimizes* the cost function $J(V)$. The optimal diffeomorphic flow F_t is then computed by integrating the ODE (4). This intricate variational problem has solutions[4,7] and can be solved numerically as a non-linear control problem, after discretization of the given reference snapshots S_0 and S_1 by finite meshes. As in Azencott *et al.*[4] our numerical solution combines *gradient descent* with a *continuation method* which progressively increases the positive weights λ and μ, while keeping a fixed ratio μ/λ. Several such computations are launched to select a good ratio μ/λ.

For normal patients, our reconstruction of MVA dynamics by analysis of 3D-Echo image sequences, requires 7–15 min of CPU on a 2.8 GHz processor. For regurgitation patients, this reconstruction requires 1–3 hours of CPU, due to the complicated creases and folds of prolapsed mitral leaflets.

METHODS: STRAIN TENSORS COMPUTATION

Recent elasticity models experimentally validated *in vivo* or *in vitro* for ovine and porcine mitral leaflet tissues are hyperlinear and non-isotropic, so it is a delicate and quite complicated task to evaluate *in vivo* and non-invasively the proper parametrization of such elasticity models for human mitral valves, in order to automatically generate patient specific leaflets elasticity models. This is one of the main reasons why we have selected mitral leaflets strain intensities (instead of stress intensities) as a robust and highly implementable non-invasive comparison tool among groups of patients. Indeed, a key point is that strain tensor computations do not require any parametric elasticity assumption on leaflets tissue, and use only computer reconstructed MVA dynamics.

For each patient,we have systematically evaluated the mitral leaflets strain tensors between the same times MS and ES, even though zero stress configurations occur at beginning systole. An important advantage of our (MS, ES) choice is that it only requires the reconstruction of leaflet deformations in the shorter time span (5 to 6 image frames in our data) betwen MS and ES. Also since we only compute strain tensors, the notion of zero stress configuration has far less importance than when one wants to study stress tensors (Figs. 5, 6, and 7).

For each one of our 3D-echo image data sets, we have computed the dynamic mitral leaflet deformations $F_t(x)$ between mid-systole MS and end-systole ES, at 1500–3000 leaflet points x of the mid-systole leaflet. The classical full 3D strain tensors $\boldsymbol{\varepsilon}(t,x)$ at $(t,\ x)$ is the symmetric 3 by 3 matrix classically given by

$$\varepsilon = \varepsilon(t,x) = \frac{1}{2}\left(\nabla u_t + \nabla u_t^*\right).$$

where $u_t(x) = F_t(x) - x$ and ∇ is the gradient operator in R^3. To characterize at time t the geometric deformations of leaflet tissue at point x, the most relevant strain tensor is the 2×2 matrix $\boldsymbol{\eta}(t,x)$, which is the restriction of $\boldsymbol{\varepsilon}(t,x)$ to the plane T_x tangent at x to the leaflet surface S_t. We define the geometric tissue strain $geoStr(x)$ at x as the square root of the ratio of areas between deformed and reference small tissue patches around x, which is also the average deformation ratio of small tissue lengths around x between MS and ES. This gives the formula

$$geoStr(x) = \sqrt{|\det(\eta(t,x))|} = \sqrt{|\lambda_1||\lambda_2|} \qquad (10)$$

where λ_1, λ_2 are the eigenvalues of $\boldsymbol{\eta}(t,x)$. The harmonic mean $geoStr(x)$ of these two eigenvalues is also the harmonic mean of the two main tissue "stretch coefficients" at x, and is insensitive to rotations of local coordinates in T_x (Fig. 8).

When $geoStr(x) > 1$, we have local surface dilation around x between times MS and ES, and when $geoStr(x) < 1$, we have local surface contraction around x. Thus large values of $|geoStr(x) - 1|$ are indicative of potential high leaflet tissue fatigue at x. So we define Local Strain Intensities $LSI(x)$ by

$$LSI(x) = |geoStr(x) - 1| \qquad (11)$$

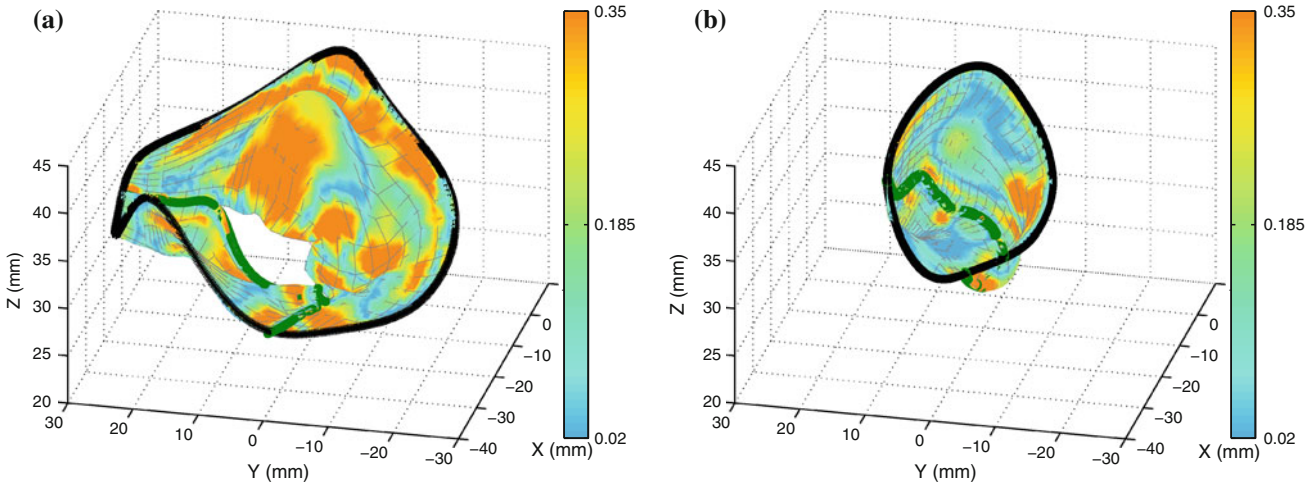

FIGURE 5. Regurgitation Case #1. Pre- and post-surgery views of both mitral leaflets at time MS, displaying the values of local strain intensities LSI. These strain intensities, which are dimensionless (see main text) are computed between times MS and ES, and are displayed on the same color scale before and after surgery. In this color coding, high strain points (in yellow and red) have LSI values larger than 0.24, while low strain points (in light and dark blue) have LSI values smaller than 0.10. Coordinates are in mm. The open regurgitation area on the pre-surgery view disappears after repair surgery. The dark green line marks the coaptation line. The thick black line is the annulus for pre-surgery display, and is the synthetic flexible annulus for post-surgery display. The synthetic annulus has smaller size than the original annulus, and hence at MS the MVA cross-section lengths along *X* or *Y* go from about 35–40 mm before surgery to about 20–25 mm after NRD surgery.

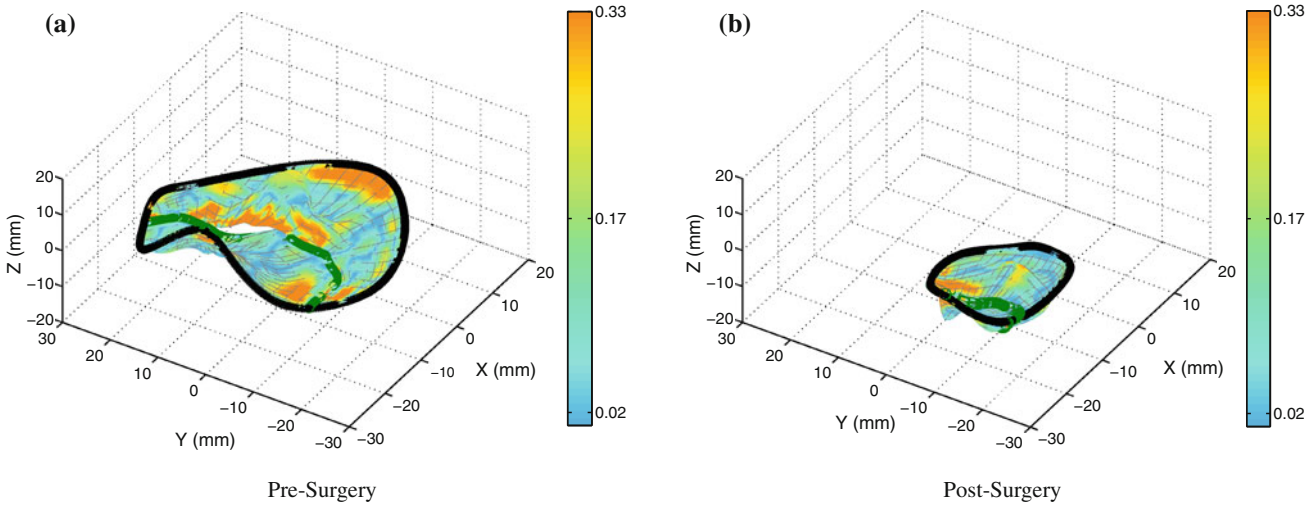

FIGURE 6. Regurgitation case #2.

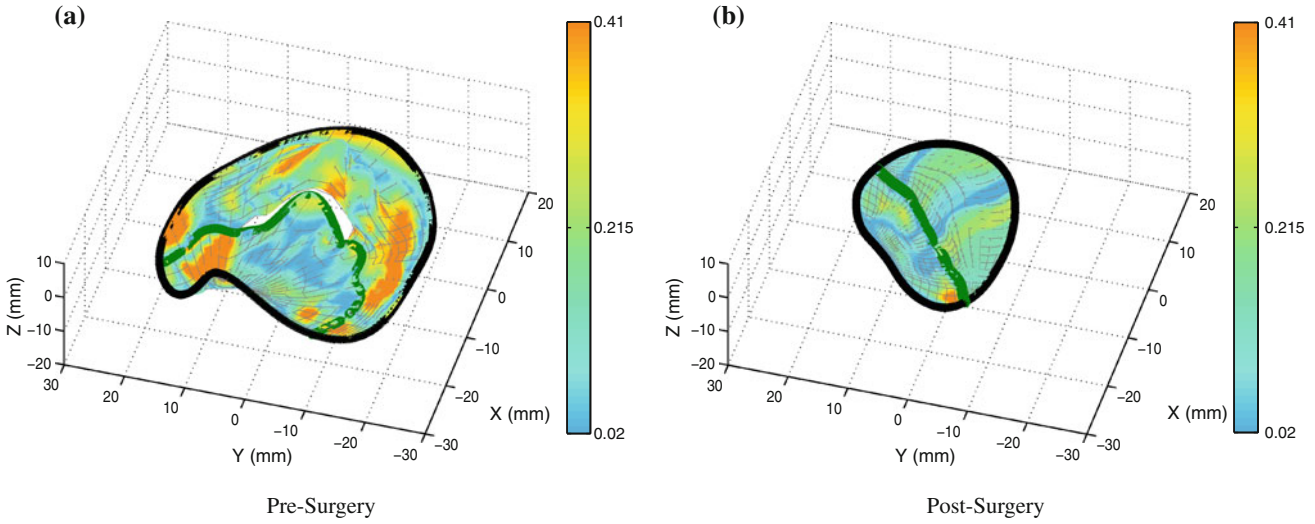

FIGURE 7. Regurgitation case #3.

The values LSI(x) are dimensionless, and quantify the local percentage of length dilation or of length contraction around leaflet point x.

METHODS : STRAIN MAPS FOR MITRAL LEAFLETS

For each patient, and each leaflet AL or PL, the local strain intensities $LSI(x)$ between MS and ES are computed at M points x of the leaflet position at time MS, with $1500 \leq M \leq 3000$. This very large list of strain intensity values is called here a "Strain Map".

To visualize strain maps, as in Fig. 8, the value $LSI(x)$ is color-coded using a fixed coding scale, and displayed at the 3D-position x. Our color 3D-graphics for strain maps are hence always displayed on 3D leaflets snapshots at time MS. These graphic displays are very efficient for fast visual inspection of the high strain areas in the MVA, as well as for easy visual comparison of strain distributions between two specific patients, or between pre-and post surgery MVAs.

Each strain map involves a large number M of strain intensities, hence the mean strain or the median strain value cannot adequately characterize strain values distributions. So, for quantified comparisons of strain maps, we compare their percentile curves. Recall that for any percentage p %, the percentile $Q(p) > 0$ of the strain map Z, is the strain intensity value "s" such that exactly p % of the M strain intensities observed in Z are inferior to s.

The accuracy of empirical strain percentiles $Q(p)$ is quite good for $10\% < p < 90\%$, since estimation errors for $Q(p)$ are then inferior to $\frac{1}{2\sqrt{M}} < 1.2\%$, but

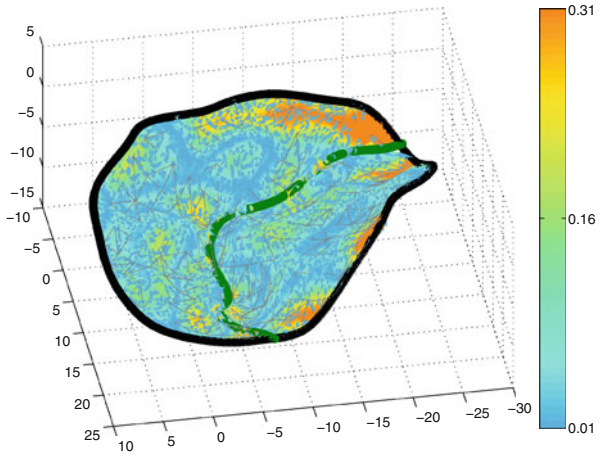

FIGURE 8. Normal Case. Display of local strain intensities, computed between MS and ES. Thick black line = Annulus, Dark Green = Coaptation line.

statistical accuracy of the $Q(p)$ becomes weaker for extreme percentiles. So to compare strain maps, we deliberately restrict ourselves to studying strain percentiles $Q(p)$ where $10\% < p < 90\%$.

We will focus below on the analysis of strain reduction effects. Strain percentile curves are particularly well suited for this analysis. Indeed, if an arbitrary linear or non-linear strain reduction function $s \to g(s) < s$ is applied to all the strain values s in a strain map Z_1, this operation generates a reduced strain map Z_2. It is easy to see that the initial strain percentiles $Q_1(p)$ are then systematically reduced, and verify $Q_2(p) \leq Q_1(p)$ for all p between 0 and 100%.

Thus to detect if a strain map Z_2 can be generated by some unknown *strain reduction* of another strain map Z_1, we simply need to check if the strain percentile functions verify $Q_2(p) \leq Q_1(p)$ for all p. In classical statistical terminology, one then says that the strain values of Z_2 are "statistically smaller" than those in Z_1.

The statistical significance of the inequality $Q_2(p) \leq Q_1(p)$ for all p is computed by the non-parametric Kolmogorov–Smirnov test (KS-test). This is a much more demanding and precise validation of strain reduction than a simple t-test applied to compare the mean strain values between 2 leaflets.

RESULTS: STRAIN COMPARISONS BETWEEN NORMAL AND REGURGITATION CASES

We have first generated two reference strain percentiles curves q_{AL} and q_{PL} for normal patients. This is done by computing for each p, the average $q_{AL}(p)$ of the strain percentiles $Q(p)$ for our 10 normal AL, and the average $q_{PL}(p)$ of strain percentiles $Q(p)$ for our 10 normal PL.

For each one of our 10 pre-surgery regurgitation cases, we have then compared the strain percentiles curves of each Al or PL leaflet to the corresponding reference strain curves q_{AL} or q_{PL}.

For 18 of our 20 pre-surgery mitral leaflets, all affected by regurgitation and prolapse, we find that pre-surgery *strain percentiles are larger* than for average normal patients (see Fig. 9). Each such positive comparison was validated by the KS-test at confidence level 95%.

For each pre-surgery regurgitation case, we define the *strain severity* of each anterior leaflet AL, by the average over "p" of the ratios $Q(p)/q_{AL}(p)$ between pre-surgery strain percentiles $Q(p)$ and the reference strain percentiles $q_{AL}(p)$. Similar definition for the strain severity of the posterior leaflet PL.

We found that for 18 of our 20 pre-surgery mitral leaflets, *strain severities were clearly larger than 1*, with strain severity values ranging from 1.05 to 1.60 for AL leaflets, and from 1.12 to 1.75 for the PL leaflets.

For the two last pre-surgery leaflets, the strain severities were equal to 0.92 and 0.97, which are not statistically distinct from the value 1, since their error margins (equal to 1 standard deviation) are of the order of 0.09.

RESULTS: LEAFLETS STRAIN REDUCTION BY NRD SURGERY

For each mitral regurgitation case, we compare pre-surgery and post-surgery leaflets strain maps. Three such regurgitation cases are displayed in Figs. 5, 6, and 7. Here strain intensities are color-coded at each leaflet point. These graphic displays show that NRD surgery generally reduces strain on each leaflet.

For both mitral leaflets of the 10 patients undergoing NRD surgery (the "NRD group"), we have quantified the strain reduction between pre- and post-surgery. For 17 of those 20 diseased leaflets, the strain reduction inequality $Q_{Post}(p) < Q_{Pre}(p)$ clearly holds between pre- and post-surgery strain percentiles, and is validated by the K-S test, indicating a generic leaflets strain reduction effect due to NRD surgery. Among the other 3 diseased leaflets, 2 leaflets exhibited a rough equality between the strain percentiles $Q_{Post}(p)$ and $Q_{Pre}(p)$, up to errors of estimation. Only 1 diseased leaflet out of 20 exhibited an increase in strain after NRD surgery. These results thus seem to confirm a generic effect of *leaflets strain reduction due to NRD surgery*

We also found that for the NRD group, post-surgery strain intensities tend to be slightly smaller than average normal strain (see Fig. 9), with frequent near equality between post-surgery strains and average normal strains.

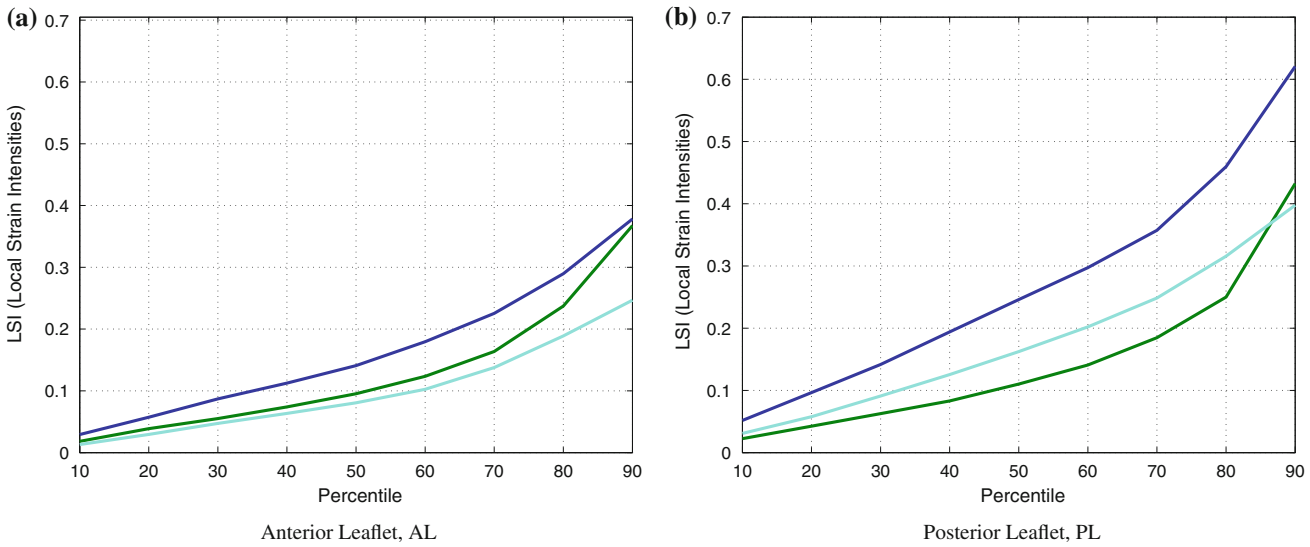

FIGURE 9. Strain percentiles curves for one pre-surgery case (dark blue), and for the associated post-surgery (light blue). We have simultaneously displayed the strain percentile curve for one normal patient (green). For typical pre-surgery regurgitation cases, our results show that the strain intensities of mitral leaflets are reduced by NRD surgery. After surgery, the strain intensities of repaired leaflets become again quite similar to those of average normal leaflets.

For each diseased AL or PL leaflet, we compute a multiplicative strain reduction factor srf (AL) or srf(PL) between pre-surgery and post-surgery. These strain reduction factors are defined as the average of the strain percentiles ratios $Q_{\text{Post}}(p)/Q_{\text{Pre}}(p)$ over all p between 10 and 90%.

We then compute a global strain reduction factor SRF as the average of the two factors srf(AL) and srf (PL). The standard deviations of errors affecting these SRF values range from 0.05 to 0.15.

Multiplicative strain reduction factors SRF were observed to be indeed inferior to 1 for nine of our ten regurgitation cases, with values ranging between 0.44 and 0.96. We observed a value SRF > 1 for only one of our 10 regurgitation cases, for which we had SRF $= 1.28$. Our strain reduction factor thus seems to offer an interesting patient specific quantification for the leaflets strain reduction achieved by NRD surgery.

CONCLUSIONS

We have focused on the computerized analysis of 3D-Echo image sequences, in order to generate patient specific modeling of the mitral valve apparatus (MVA) at two reference times MS and ES, and in order to accurately reconstruct the MVA deformations between MS and ES. Our goal was to to compute and compare mitral leaflets strain values between MS and ES.

We have introduced a 3D-image registration technique by diffeomorphic deformations, well adapted to the tracking of two thin deformable surfaces (the mitral leaflets and their natural boundaries).

Our approach shows that mitral leaflets strain values are much easier to compute than stress values, and certainly require much less detailed biological information about patient specific elasticity characteristics of mitral leaflet tissue. Indeed, strain computations depend only on the computerized reconstruction of leaflets geometry and of their actual deformations, while stress computations require a fully parametrized patient specific elasticity model of human mitral valves.

We have compared leaflets strain distributions between three groups of patients: normal, pre-surgery regurgitation cases, and corresponding post-surgery cases. Our main statistical tool for comparing leaflets strain distributions is to compare their associated strain percentiles curves. Typically strain reduction forces a decrease in the observed strain percentiles curves. For each regurgitation case, we quantify the strain reduction effect of mitral valve repair surgery by computing the average ratios of matching strain percentiles.

Our results, based on the computerized analysis of leaflets strain in 10 normal cases, 10 pre-surgery cases, and 10 associated post-surgery cases, show that for 90% of our regurgitation cases, the strain values tends to be statistically larger than for the average normal cases.

Moreover, we have presented tangible evidence that NRD mitral valve repair surgery generally tends to reduce leaflet strain values, and typically brings them down slightly below average normal strain levels. We have proposed a computable patient specific Strain Reduction Factor to quantify the reduction of leaflets

strain achieved by NRD surgery in each specific case of mitral regurgitation repair surgery.

We are aware that at this stage, our computational methods have not yet been validated experimentally by *in vivo* strain measurements on human patients, or more plausibly by *in vivo* ovine or porcine mitral leaflets strain evaluations. Nevertheless, our approach already has the merit of being patient specific, and of being immediately applicable to standard clinical image data acquired non-invasively by 3D echocardiography of incoming mitral valve patients.

Our patient specific geometric and deformations modeling effort for human mitral valves is a first step toward software development enabling virtual evaluation of surgical techniques designed to acutely decrease mitral valve strain and to improve long-term durability of surgical mitral valve repair.

ACKNOWLEDGMENTS

We acknowledge support by grant NSF-0811133 in 2008-2011 and by the John and Marynane McCormack Cardiology Fund (2009–2011). We thank Dr Jane Grande-Allen (Rice Univ., Bio-Engineering) for helpful comments regarding mitral valve elasticity.

REFERENCES

[1]Altiok, E., S. Hamada, S. van Hall, M. Hanenberg, G. Dohmen, M. Almalla, E. Grabskaya, M. Becker, N. Marx, and R. Hoffmann. Comparison of direct planimetry of mitral valve regurgitation orifice area by 3D transesophageal echocardiography to effective regurgitant orifice area obtained by proximal flow convergence method. *Am. J. Cardiol.* 107(3):452–458, 2011.

[2]Azencott, R. Elastic Deformations of Soft 3D-shapes, IBIS Colloquium on Medical Image Analysis. Kiawah Island: The Methodist Hospital, 2006.

[3]Azencott, R., R. Glowinski, and A. Ramos. A controllability approach to shape identification. *Appl. Math. Lett.* 21:861–865, 2008.

[4]Azencott R., R. Glowinski, J. He, R. Hoppe, A. Jajoo, Y. Li, A. Martynenko, R. Hoppe, S. Ben Zekry, S. Little, and W. Zoghbi. Diffeomorphic matching and dynamic deformable surfaces in 3D medical imaging. *Comput. Methods Appl. Math.* 10:235–274, 2010.

[5]Baraldi, P., A. Sarti, C. Lamberti, A. Prandini, and F. Sgallari. Evaluation of differential optical flow techniques on synthesized echo images. *IEEE Trans. Biomed. Eng.* 43:259-272, 1996.

[6]Barron, J., D. Fleet, and S. Beauchemin. Performance of optical flow techniques. *Int. J. Comput. Vis.* 12:43–47, 1994.

[7]Beg, M. F., M. I. Miller, A. Trouvé, and L. Younes. Computing large deformations metric mappings via geodesic flows of diffeomorphisms. *Int. J. Comput. Vis.* 61:139–157, 2005.

[8]Beg, M. F., M. I. Miller, A. Trouv, and L. Younes. Computing large deformations metric mappings via geodesic flows of diffeomorphisms. *Int. J. Comput. Vis.* 61:139–157, 2005.

[9]Behar, V., D. Adam, P. Lysyansky, and Z. Friedman. The combined effect of non-linear filtration and window size on the accuracy of tissue displacement estimation using detected echo signals. *Ultrasonics* 41:743–753, 2004.

[10]Boukerroui, D., A. Noble, and M. Brady. Velocity estimation in ultrasound images: a block matching approach. Proc. 18th ICIPMI., Ambleside, UK, 2003, pp. 586–598.

[11]Chandra, S., I. S. Salgo, L. Sugeng, L. Weinert, S. H. Settlemier, V. Mor-Avi, and R. M. Lang. A three-dimensional insight into the complexity of flow convergence in mitral regurgitation: adjunctive benefit of anatomic regurgitant orifice area. *Am. J. Physiol. Heart Circ. Physiol.* 301(3):H1015–H1024, 2011.

[12]Cohen, B., and I. Dinstein. New maximum likelihood motion estimation schemes for noisy ultrasound images. *Pattern Recogn.* 35:455–463, 2002.

[13]Elen, A., H. F. Choi, D. Loeckx, H. Gao, P. Claus, P. Suetens, F. Maes, and J. D'hooge. Three-dimensional cardiac strain estimation using spatio-temporal elastic Registration of Ultrasound Images. *IEEE Trans. Med. Imaging* 27(11):1580–1591, 2008.

[14]Enriquez-Sarano, M., L. J. Sinak, A. J. Tajik, K. R. Bailey, and J. B. Seward. Changes in effective regurgitant orifice throughout systole in patients with mitral valve prolapse. *Circulation* 92:2951–2958, 1995.

[15]Glaunès, J., A. Qiu, M. I. Miller, and L. Younes. Large deformation diffeomorphic metric curve mapping. *Int. J. Comput. Vis.* 80:317–336, 2008.

[16]Guo, H., A. Rangarajan, S. Joshi, and L. Younes. Non-rigid registration of shapes via diffeomorphic point matching. Proc. Int. Symp. on Biomed. Imaging: From Nano to Macro, Washington, D.C., 2004, pp. 924–927.

[17]Guo, H., A. Rangarajan, and S. Joshi: Diffeomorphic point matching. In: Handbook of Mathematical Models in Computer Vision. Springer, Berlin, 2006, pp. 205–219.

[18]Heyde, B., S. Cygan, H. F. Choi, B. Lesniak-Plewinska, D. Barbosa, A. Elen, P. Claus, D. Loeckx, K. Kaluzynski, and J. D'hooge. Three-dimensional cardiac motion and strain estimation. IEEE International Ultrasonics Symposium Proceedings, 2010, pp. 1534–1537.

[19]Jimenez, J., D. Soerensen, Z. He, S. He, and A. Yoganathan. Effects of a saddle shaped annulus on mitral valve function and chordal force distribution: an in vitro study. *Ann. Biomed. Eng.* 31:1171–1181, 2003.

[20]Joshi, S., and M. Miller. Landmark matching via large deformation diffeomorphisms. *IEEE Trans. Image Process.* 9:1357–1370, 2000.

[21]Krishnamurthy, G., D. B. Ennis, A. Itoh, W. Bothe, J. C. Swanson, M. Karlsson, E. Kuhl, D. C. Miller, Jr., and N. B. Ingels. Material properties of the ovine mitral valve anterior leaflet in vivo from inverse finite element analysis. *Am. J. Physiol. Heart Circ. Physiol.* 295:1141–1149, 2008.

[22]Kunzelman, K.S., and R. P. Cochran. Stress/strain characteristic of porcine mitral valve tissue: parallel versus perpendicular collagen orientation. *J. Card. Surg.* 7(1):71–78, 1992.

[23]Kunzelman, K. S., M. S. Reimink, E. D. Verrier, and R. P. Cochran. Replacement of mitral valve posterior chordae tendineae with expanded polytetrafluoroethylene suture: a finite element study. *J. Card. Surg*. 11(2):136–145, 1996.
[24]Kunzelman, K. S., M. S. Reimink, and R. P. Cochran. Annular dilatation increases stress in the mitral valve and delays coaptation: a finite element computer model. *Cardiovasc. Surg*. 5:427–434, 1997.
[25]Kybic, J., and M. Unser Fast parametric elastic image registration. *IEEE Trans. Imag. Proc*. 12:1427–1442, 2003.
[26]Lawrie, G. Mitral valve repair vs replacement. *Cardiol. Clin*. 16(3):437–448, 1998.
[27]Lawrie, G. Mitral valve: toward complete repairability. *Surg. Technol. Int*. 15:189–197, 2006.
[28]Ledesma-Carbayo, M., J. Kybic, M. Desco, A. Santos, M. Sühling, P. Hunziker, and M. Unser. Spatio-temporal nonrigid registration for ultrasound cardiac motion estimation. *IEEE Trans. Med. Imag*. 24:1113–1126, 2005.
[29]Miller, I., A. Trouvé, and L. Younes. On the metrics and Euler-Lagrange equations of computational anatomy. *Ann. Rev. Biomed. Eng*. 4:375–405, 2002.
[30]Piegl, L., and W. Tiller. The NURBS Book. Berlin: Springer-Verlag, 1997.
[31]Prot, V., R. Haaverstad, and B. Skallerud. Finite element analysis of the mitral apparatus: annulus shape effect and chordal force distribution. *Biomech. Model. Mechanobiol*. 8:43–55, 2009.
[32]Revell, J., M. Mirmehdi, and D. McNally. Computer vision elastography: speckle adaptive motion estimation for elastography using ultrasound sequences. *IEEE Trans. Med. Imag*. 24:755–760, 2005.
[33]Strintzis, M. G., and I. Kokkinidis. Likelihood motion estimation in ultrasound image sequences. *IEEE Sig. Proc. Lett*. 4:156–157, 1997.
[34]Suhling, M., M. Arigovindan, C. Jansen, P. Hunziker, and M. Unser. Myocardial motion analysis from B-mode echocardiograms. *IEEE Trans. Imag. Proc*. 14:525–536, 2005.
[35]Yong, Y., J. Clark, and D. Khoury. Speckle tracking in intracardiac echocardiography for the assessment of myocardial deformation. *IEEE Trans. Biomed. Eng*. 56:416–425.
[36]Zienkiewicz, O. C., and R. L. Taylor. Finite element method for solid and structural mechanics. (6th edition). Elsevier (2005), 631 pp.